Analytic calculations of hyper-Raman spectra from density functional theory hyperpolarizability gradients

Magnus Ringholm, Radovan Bast, Luca Oggioni, Ulf Ekström, and Kenneth Ruud

Citation: The Journal of Chemical Physics **141**, 134107 (2014); doi: 10.1063/1.4896606
View online: http://dx.doi.org/10.1063/1.4896606
View Table of Contents: http://scitation.aip.org/content/aip/journal/jcp/141/13?ver=pdfcov
Published by the AIP Publishing

Analytic calculations of hyper-Raman spectra from density functional theory hyperpolarizability gradients

Magnus Ringholm,[1] Radovan Bast,[2,3] Luca Oggioni,[1,4] Ulf Ekström,[5] and Kenneth Ruud[1]
[1]*Centre for Theoretical and Computational Chemistry, Department of Chemistry, University of Tromsø – The Arctic University of Norway, 9037 Tromsø, Norway*
[2]*Theoretical Chemistry and Biology, School of Biotechnology, Royal Institute of Technology, AlbaNova University Center, S-10691 Stockholm, Sweden*
[3]*PDC Center for High Performance Computing, Royal Institute of Technology, S-10044 Stockholm, Sweden*
[4]*Department of Physics G. Occhialini, University of Milano Bicocca, Piazza della scienza 3, 20126 Milan, Italy*
[5]*Centre for Theoretical and Computational Chemistry, Department of Chemistry, University of Oslo, P.O. Box 1033 Blindern, 0315 Oslo, Norway*

(Received 28 June 2014; accepted 16 September 2014; published online 3 October 2014)

We present the first analytic calculations of the geometrical gradients of the first hyperpolarizability tensors at the density-functional theory (DFT) level. We use the analytically calculated hyperpolarizability gradients to explore the importance of electron correlation effects, as described by DFT, on hyper-Raman spectra. In particular, we calculate the hyper-Raman spectra of the all-trans and 11-cis isomers of retinal at the Hartree-Fock (HF) and density-functional levels of theory, also allowing us to explore the sensitivity of the hyper-Raman spectra on the geometrical characteristics of these structurally related molecules. We show that the HF results, using B3LYP-calculated vibrational frequencies and force fields, reproduce the experimental data for all-trans-retinal well, and that electron correlation effects are of minor importance for the hyper-Raman intensities. © *2014 AIP Publishing LLC*. [http://dx.doi.org/10.1063/1.4896606]

I. INTRODUCTION

The phenomenon of hyper-Raman scattering (HRS) was first proposed theoretically in the late 1950s.[1] It is a nonlinear scattering process where two incident photons of frequency ω stimulate the emission of a photon of frequency $2\omega \pm \omega_t$, where ω_t is a frequency associated with a vibrational transition in the system being studied. The process can thus be considered an inelastic scattering process related to the second-harmonic generation effect. In non-resonant HRS, which is the subject of this work, the frequency $2\omega \pm \omega_t$ is well separated from any electronic transitions in the system. Hyper-Raman scattering was first observed experimentally in the 1960s.[2] Because it is the geometrical variations of the molecular first hyperpolarizability that govern the HRS spectral intensities, HRS represents a scattering process with different selection rules than that of regular Raman spectroscopy. For the latter spectroscopy, the geometrical variations of the molecular polarizability is the governing quantity. The scattering process and the involvement of the first hyperpolarizability in HRS allow for the enhancement of other vibrational modes than those observed, for instance, in infrared absorption or Raman spectroscopy.[3–5] Furthermore, HRS is well suited for the study of low-frequency vibrational modes, which has traditionally been a difficult region for other spectroscopies because of instrumental limitations, although we note that these limitations are gradually being lifted in the case of (chiroptical) Raman spectroscopy.[6]

Hyper-Raman scattering is not as well known or frequently used as, e.g., infra-red (IR) or Raman spectroscopy, mainly because the signal is significantly weaker than the corresponding Raman signal due to its multiphoton nature (it is typically several orders of magnitude weaker than non-resonant Raman scattering[7]). Furthermore, the experimental setup for the HRS is more complicated than a regular Raman instrument. The literature on experimental HRS is therefore rather limited, though it is in principle accessible with any experimental equipment designed to measure hyper-Rayleigh scattering.

The calculation of hyper-Raman cross sections requires the calculation of first-order geometrical derivatives of the molecular first hyperpolarizability with respect to displacements along the normal coordinates of the system. This corresponds to a fourth-order quasi-energy derivative and carries substantial computational complexity. A few theoretical studies of HRS have been presented in the literature, and in particular Champagne and co-workers[8–10] have pioneered the theoretical calculation of HRS spectra. More recently, Ågren and co-workers have also presented theoretical studies of HRS.[5] However, all analytic calculations of the hyperpolarizability gradients in previous studies have been restricted to the Hartree-Fock (HF) level of theory.

In this work, we use recent developments in the analytic calculation of molecular properties[11–13] to present the first analytic calculations of hyperpolarizability gradients at the density-functional theory (DFT) level. We apply the new methodology to the calculation of hyper-Raman spectra for the *all-trans* and 11-*cis* isomers of retinal. These systems have been selected in part because of the availability of experimental data for the *all-trans* isomer,[14] but also because these systems would allow us to theoretically explore the sensitivity of HRS to structural differences, in this particular case to

cis/trans isomerism. We will also explore the importance of electron correlation effects, as described by DFT, for the HRS scattering cross sections.

The rest of the paper is organized as follows: We first give an introduction to the theory of HRS and the computational approach used to calculate the required first-order geometrical derivatives of the first hyperpolarizabilities, with special emphasis on the exchange–correlation (XC) contributions. We then give some details of the hyper-Raman calculations on the retinal isomers studied, before turning to a discussion of the results of the calculations. Finally, we give some concluding remarks.

II. THEORY

The foundations of hyper-Raman spectroscopy, the calculation of HRS cross sections, and the evaluation of the relevant geometrical hyperpolarizability derivatives have been discussed previously.[5,8–10] As the main difference between DFT and HF will be in the evaluation of the exchange–correlation contributions, we will here follow our earlier exposition of the analytic evaluation of the gradients of the first hyperpolarizability at the HF level,[5] providing an outline of the general energy-derivative theory framework but with the main focus given to the new and nontrivial exchange–correlation contributions. However, in order to establish the notation and provide the background for the quantities we need to evaluate, we first give a brief introduction to the expressions for the HRS cross sections.

A. Hyper-Raman scattering cross sections

When a sample is exposed to an incident laser field of frequency ω and intensity $\mathbf{I}_0$, the Stokes hyper-Raman intensity at the frequency $(2\omega - \omega_t)$ for a vibrational transition t of frequency ω_t is given by[8–10]

$$\mathbf{I}_{hR,t}(2\omega-\omega_t) \propto N\mathbf{I}_0^2(2\omega-\omega_t)^4|\langle\Psi_{\text{init}}|\beta(\omega,\mathbf{Q})|\Psi_{\text{fin}}\rangle|^2, \tag{1}$$

where we have introduced the initial and final states of the system $|\Psi_{\text{init}}\rangle$ and $|\Psi_{\text{fin}}\rangle$, respectively, N denoting the population of the ground state. $\beta(\omega,\mathbf{Q})$ is here the first hyperpolarizability at the frequency ω, and it is a function of the nuclear displacements along the normal coordinates $\mathbf{Q}$. We use the Born–Oppenheimer approximation to write the initial and final states as products of pure vibrational and electronic states, neglecting vibronic couplings which may, however, be important close to or at electronic resonances. If $(2\omega - \omega_t)$ is detuned from electronic resonance, the electronic state of both the initial and final state can be taken to be the ground state, so that we can integrate over the electronic degrees of freedom to obtain

$$\mathbf{I}_{hR,t}(2\omega-\omega_t) \propto N\mathbf{I}_0^2(2\omega-\omega_t)^4|\langle n|\overline{\beta}(\omega,\mathbf{Q})|p\rangle|^2. \tag{2}$$

In Eq. (2), the initial and final vibrational states are denoted by $|n\rangle$ and $|p\rangle$, respectively. Also introduced is the electronic first hyperpolarizability $\overline{\beta}$ of the electronic ground state, where we have indicated that the electronic hyperpolarizability is a function of the frequency of the incoming light ω and the nuclear positions $\mathbf{Q}$. The vibrational potential and geometry dependence of the first hyperpolarizability can be expanded in a Taylor series around the equilibrium geometry with respect to displacements along the normal modes Q_i of the system. Using Greek subscripts for Cartesian axes, the expansions around the equilibrium geometry can be written

$$\begin{aligned}\beta_{\alpha\beta\gamma}(\mathbf{Q}) = \overline{\beta}^0_{\alpha\beta\gamma} + \sum_a \Bigg[&\left(\frac{\partial\overline{\beta}_{\alpha\beta\gamma}}{\partial Q_a}\right)_{\text{eq}} Q_a \\ &+ \frac{1}{2}\sum_b \left(\left(\frac{\partial^2\overline{\beta}_{\alpha\beta\gamma}}{\partial Q_a \partial Q_b}\right)_{\text{eq}} Q_a Q_b \right. \\ &\left. + \frac{1}{3!}\sum_c \left(\frac{\partial^3\overline{\beta}_{\alpha\beta\gamma}}{\partial Q_a \partial Q_b \partial Q_c}\right)_{\text{eq}} Q_a Q_b Q_c + \cdots\right)\Bigg],\end{aligned} \tag{3}$$

and

$$\begin{aligned}V(\mathbf{Q}) = V^{(0)}_{\text{eq}} + \frac{1}{2}\sum_a\sum_b \Bigg(&V^{(2)}_{\text{eq, ab}} Q_a Q_b \\ &+ \frac{1}{3!}\sum_c V^{(3)}_{\text{eq, abc}} Q_a Q_b Q_c + \cdots\Bigg),\end{aligned} \tag{4}$$

where the ith order derivative of the energy at the equilibrium geometry is $V^{(i)}_{\text{eq},\ldots}$. We note that $V^{(1)}_{\text{eq, a}} = 0$ since the expansion is carried out at the equilibrium geometry. In the present work, we use the double-harmonic approximation,[8] where the expansions in Eqs. (3) and (4) are truncated after the first- and second-order derivatives, respectively. The latter truncation means that the vibrational wavefunctions correspond to harmonic oscillator wavefunctions.

With these expansions and truncations, Eq. (2) can in the double-harmonic approximation be written as

$$\begin{aligned}&\mathbf{I}_{hR,t}(2\omega-\omega_t) \\ &\quad\propto N\mathbf{I}_0^2(2\omega-\omega_t)^4\left(\frac{\partial\overline{\beta}(-2\omega;\omega,\omega)}{\partial Q_t}\right)^2_{\text{eq}}|\langle n|Q_t|p\rangle|^2.\end{aligned} \tag{5}$$

From the properties of the harmonic oscillator vibrational wavefunctions, the only nonzero contributions in Eq. (5) come from transitions between neighboring vibrational states,[15] i.e., states that differ by at most one vibrational quantum. By considering the polarization of the incoming and scattered light, Eq. (5) can be further specialized to the final expressions[9,10] for the hyper-Raman scattering cross sections for either vertically (V) or horizontally (H) plane-polarized incident light, respectively, at the frequency $(2\omega - \omega_a)$

$$\begin{aligned}&\mathbf{I}^{VV}_{hR,a}(2\omega-\omega_a) \\ &\quad\propto N\hbar\mathbf{I}_0^2\frac{(2\omega-\omega_a)^4}{2\omega_a[1-\exp(-\hbar\omega_a/kT)]}\langle\tilde{\beta}'^2_{\alpha\alpha\alpha}(\omega,Q_a)\rangle,\end{aligned} \tag{6}$$

and

$$\begin{aligned}&\mathbf{I}^{HV}_{hR,a}(2\omega-\omega_a) \\ &\quad\propto N\hbar\mathbf{I}_0^2\frac{(2\omega-\omega_a)^4}{2\omega_a[1-\exp(-\hbar\omega_a/kT)]}\langle\tilde{\beta}'^2_{\alpha\beta\beta}(\omega,Q_a)\rangle,\end{aligned} \tag{7}$$

where the second index in VV and HV means that we consider only the vertically plane-polarized scattered light. Here, k denotes the Boltzmann constant and T the temperature, which enter into the Boltzmann term in Eqs. (6) and (7) in order to take the population of the excited vibrational states into account. In Eqs. (6) and (7), we have also introduced the averages $\langle\tilde{\beta}'^2_{\alpha\alpha\alpha}(\omega, Q_a)\rangle$ and $\langle\tilde{\beta}'^2_{\alpha\beta\beta}(\omega, Q_a)\rangle$, which, defining

$$\beta'_{\alpha\beta\gamma} \equiv \left(\frac{\partial\overline{\beta}_{\alpha\beta\gamma}(-2\omega;\omega,\omega)}{\partial Q_a}\right)_{\text{eq}}, \tag{8}$$

can be expressed as

$$\begin{aligned}\left\langle\tilde{\beta}'^2_{\alpha\alpha\alpha}\right\rangle =& \frac{1}{7}\sum_{\alpha}^{x,y,z}\beta'^2_{\alpha\alpha\alpha} \\ &+ \frac{1}{35}\sum_{\alpha,\beta\neq\alpha}^{x,y,z}\left(4\beta'^2_{\alpha\alpha\beta} + 2\beta'_{\alpha\alpha\alpha}\beta'_{\alpha\beta\beta} + 4\beta'_{\beta\alpha\alpha}\beta'_{\alpha\alpha\beta}\right. \\ &\left. + 4\beta'_{\alpha\alpha\alpha}\beta'_{\beta\beta\alpha} + \beta'^2_{\beta\alpha\alpha}\right) \\ &+ \frac{1}{105}\sum_{\alpha,\beta\neq\alpha,\gamma\neq\alpha,\beta}^{x,y,z}\left(4\beta'_{\alpha\alpha\beta}\beta'_{\beta\gamma\gamma} + \beta'_{\beta\alpha\alpha}\beta'_{\beta\gamma\gamma}\right. \\ &\left. + 4\beta'_{\alpha\alpha\beta}\beta'_{\gamma\gamma\beta} + 2\beta'^2_{\alpha\beta\gamma} + 4\beta'_{\alpha\beta\gamma}\beta'_{\beta\alpha\gamma}\right)\end{aligned} \tag{9}$$

and

$$\begin{aligned}\left\langle\tilde{\beta}'^2_{\alpha\beta\beta}\right\rangle =& \frac{1}{35}\sum_{\alpha}^{x,y,z}\beta'^2_{\alpha\alpha\alpha} \\ &+ \frac{1}{105}\sum_{\alpha,\beta\neq\alpha}^{x,y,z}\left(4\beta'_{\alpha\alpha\alpha}\beta'_{\alpha\beta\beta} - 6\beta'_{\alpha\alpha\alpha}\beta'_{\beta\beta\alpha}\right. \\ &\left. + 8\beta'^2_{\alpha\alpha\beta} + 9\beta'^2_{\alpha\beta\beta} - 6\beta'_{\alpha\alpha\beta}\beta'_{\beta\alpha\alpha}\right) \\ &+ \frac{1}{105}\sum_{\alpha,\beta\neq\alpha,\gamma\neq\alpha,\beta}^{x,y,z}\left(3\beta'_{\alpha\beta\beta}\beta'_{\alpha\gamma\gamma} - 2\beta'_{\alpha\alpha\gamma}\beta'_{\beta\beta\gamma}\right. \\ &\left. - 2\beta'_{\alpha\alpha\beta}\beta'_{\beta\gamma\gamma} + 6\beta'^2_{\alpha\beta\gamma} - 2\beta'_{\alpha\beta\gamma}\beta'_{\beta\alpha\gamma}\right).\end{aligned} \tag{10}$$

From these equations, it is clear that in order to perform a hyper-Raman analysis by Eqs. (6) and (7), the normal modes of the system and their (harmonic) fundamental vibrational frequencies must be determined. Furthermore, the hyperpolarizability derivatives appearing in Eqs. (8)–(10) must be calculated. We now turn to the analytic evaluation of the gradient of the first dipole hyperpolarizability in an atomic-orbital-based approach.

B. The gradient of the first hyperpolarizability

In earlier theoretical studies of hyper-Raman spectra,[5,8,9] with the exception of one study in which also the (static) first hyperpolarizability gradients were calculated at the Møller–Plesset (MP) level of theory,[10] HRS spectra have been calculated using gradients of the first hyperpolarizability calculated at the HF level. We here extend these earlier studies to evaluate the importance of electron correlation effects on the hyper-Raman scattering cross sections as described by DFT, presenting the first analytic implementation of the first hyperpolarizability gradient at the DFT level. The implementation is formally an extension to the DFT level of theory of the approach we have used for HF wave functions.[5] However, we have recently implemented an open-ended formulation[16] of response theory. The theoretical treatment of the routines in this implementation[11] allows the identification and evaluation of contributions to perturbed Fock and density matrices and the various contributions to a given response property in a recursive manner, where the principal limitation on which properties that can be calculated stems from the limitations of associated routines for perturbed 1-electron and 2-electron integrals and routines for exchange–correlation contributions. Thus, even though we here for simplicity will present the working equations for the first hyperpolarizability gradients, with a particular emphasis on the exchange–correlation contributions, the theoretical treatment of the routines in the present implementation is much more generic and does not require a tailored routine for the evaluation of this property.

A linear response property $\langle\langle A; B\rangle\rangle_{\omega_b}$ can be expressed as a time-averaged quasienergy Lagrangian perturbation-strength derivative[16] L^{ab}

$$\langle\langle A; B\rangle\rangle_{\omega_b} = \left.\frac{\mathrm{d}\{\tilde{L}^a(\tilde{\mathbf{D}}, t)\}_T}{\mathrm{d}\varepsilon_b}\right|_{\{\varepsilon\}=0} = L^{ab}; \qquad \omega_a = -\omega_b, \tag{11}$$

where ϵ_b denotes a perturbation strength, superscripts denote perturbation-strength differentiation with respect to perturbations a and b (and in general also other perturbations) with associated frequencies ω_a and ω_b, $\tilde{\mathbf{D}}$ is the density matrix considered at general perturbation strengths (in general, a tilde will be used when considering a quantity at general perturbation strengths, and no tilde is used when the quantity is evaluated at zero perturbation strengths). The braces $\{\}_T$ denote time-averaging over a full period of the applied perturbation. In Eq. (11), we have introduced the quasi-energy Lagrangian gradient

$$\tilde{L}^a(\tilde{\mathbf{D}}, t) \overset{\{\mathrm{Tr}\}_T}{=} \tilde{\mathcal{E}}^{0,a} - \tilde{\mathbf{S}}^a\tilde{\mathbf{W}}, \tag{12}$$

where $\overset{\{\mathrm{Tr}\}_T}{=}$ is used to denote that we take the trace of the matrix products on the right-hand side and perform time averaging of the quantities over a period of the applied perturbation. In Eq. (12), the overlap integral matrix $\mathbf{S}$ and generalized energy-weighted density matrix $\mathbf{W}$ were also introduced, where

$$\tilde{\mathbf{W}} = \tilde{\mathbf{D}}\tilde{\boldsymbol{\mathcal{F}}}\tilde{\mathbf{D}} + \tfrac{i}{2}\left(\dot{\tilde{\mathbf{D}}}\tilde{\mathbf{S}}\tilde{\mathbf{D}} - \tilde{\mathbf{D}}\tilde{\mathbf{S}}\dot{\tilde{\mathbf{D}}}\right). \tag{13}$$

Here, the dot in $\dot{\tilde{\mathbf{D}}}$ denotes time differentiation, and the Kohn–Sham matrix $\tilde{\boldsymbol{\mathcal{F}}}$ in the presence of an external electric field was introduced, and is given by

$$\tilde{\boldsymbol{\mathcal{F}}} = \tilde{\mathbf{h}} + \tilde{\mathbf{G}}^{\gamma}(\tilde{\mathbf{D}}) - \mathbf{F}\cdot\tilde{\boldsymbol{\mu}} + \tilde{\boldsymbol{\mathcal{F}}}_{\text{xc}}. \tag{14}$$

In Eq. (12), the Kohn-Sham energy $\tilde{\mathcal{E}}$ in the presence of an external electric field $\mathbf{F}$ was also introduced, and is given as

$$\tilde{\mathcal{E}} \overset{\{\mathrm{Tr}\}_T}{=} \left(\tilde{\mathbf{h}} - \mathbf{F}\cdot\tilde{\boldsymbol{\mu}} + \tfrac{1}{2}\tilde{\mathbf{G}}^{\gamma}(\tilde{\mathbf{D}})\right)\tilde{\mathbf{D}} + \tilde{E}_{\text{xc}}[\tilde{\rho}(\tilde{\mathbf{D}})] + \tilde{h}_{nuc}. \tag{15}$$

The energy $\tilde{\mathcal{E}}$ is dependent on the density matrix, $\tilde{\mathbf{D}}$, and both $\tilde{\mathcal{E}}$ and $\mathbf{D}$ are in general dependent on the applied perturbations,

and any differentiation of the energy may therefore entail applications of the chain rule involving $\tilde{\mathbf{D}}$. It is for this purpose that the zero superscript in $\tilde{\mathcal{E}}^{0,a}$ is introduced, denoting the number of such applications of the chain rule, so that, in general

$$\boldsymbol{\mathcal{E}}^{m,abc} = \frac{\partial^{m+3}\mathcal{E}}{(\partial \mathbf{D}^{\mathrm{T}})^m \partial\varepsilon_a \partial\varepsilon_b \partial\varepsilon_c}. \tag{16}$$

In Eqs. (14) and (15), we introduced the one-electron integral matrices $\tilde{\mathbf{h}}$ and $\mathbf{F}\cdot\tilde{\boldsymbol{\mu}}$, where $\boldsymbol{\mu}$ is the electric dipole integral matrix. We have also introduced the two-electron integral matrix with γ-scaled exchange contribution

$$\tilde{G}^{\gamma}_{\mu\nu}(\mathbf{M}) = \sum_{\alpha\beta} M_{\beta\alpha}(\tilde{g}_{\mu\nu\alpha\beta} - \gamma\tilde{g}_{\mu\beta\alpha\nu}), \tag{17}$$

the nuclear potential contribution $\tilde{h}_{nuc}$, and the exchange-correlation potential matrix $\tilde{\boldsymbol{\mathcal{F}}}_{\mathrm{xc}}$, in the adiabatic approximation connected to the exchange–correlation energy density $\tilde{\epsilon}_{\mathrm{xc}}(\tilde{\rho}(\mathbf{r}))$ through

$$(\tilde{\mathcal{F}}_{\mathrm{xc}})_{\mu\nu} = \int \mathrm{d}\mathbf{r}\, \frac{\partial\tilde{\epsilon}_{\mathrm{xc}}(\mathbf{r})}{\partial\tilde{\rho}(\mathbf{r})}\frac{\partial\tilde{\rho}(\mathbf{r})}{\partial\tilde{D}_{\nu\mu}}. \tag{18}$$

We also introduced the exchange–correlation energy $\tilde{E}_{\mathrm{xc}}[\tilde{\rho}(\tilde{\mathbf{D}})]$. The scaling factor introduced in Eq. (17) allows us to include Hartree–Fock theory ($\gamma = 1$), non-hybrid DFT ($\gamma = 0$) as well as hybrid DFT theories in which γ can take intermediate values between these two extremes, in the same theoretical framework.

In general, response properties can be expressed as quasienergy Lagrangian derivatives $L^{abc\cdots}$ evaluated at zero perturbation strength

$$L^{a} \overset{\{\mathrm{Tr}\}_T}{=} \mathcal{E}^{0,a} - \mathbf{S}^{a}\mathbf{W}, \tag{19}$$

$$\langle\langle A; B\rangle\rangle_{\omega_b} = L^{ab} \overset{\{\mathrm{Tr}\}_T}{=} \mathcal{E}^{0,ab} + \boldsymbol{\mathcal{E}}^{1,a}\mathbf{D}^{b} - \mathbf{S}^{ab}\mathbf{W} - \mathbf{S}^{a}\mathbf{W}^{b}, \tag{20}$$

$$\begin{aligned}\langle\langle A; B, C\rangle\rangle_{\omega_b,\omega_c} = L^{abc} \overset{\{\mathrm{Tr}\}_T}{=}\ & \mathcal{E}^{0,abc} + \boldsymbol{\mathcal{E}}^{1,ac}\mathbf{D}^{b} \\ & + \boldsymbol{\mathcal{E}}^{1,ab}\mathbf{D}^{c} + \boldsymbol{\mathcal{E}}^{2,a}\mathbf{D}^{b}\mathbf{D}^{c} \\ & + \boldsymbol{\mathcal{E}}^{1,a}\mathbf{D}^{bc} - \mathbf{S}^{abc}\mathbf{W} - \mathbf{S}^{ab}\mathbf{W}^{c} \\ & - \mathbf{S}^{ac}\mathbf{W}^{b} - \mathbf{S}^{a}\mathbf{W}^{bc}.\end{aligned} \tag{21}$$

We note that the expressions for the response properties in Eqs. (19)–(21) are said to follow the $(n + 1)$ rule. Other choices of rule are in general possible,[17,18] but are not the best choice for the first-order geometrical derivative of the molecular first hyperpolarizability $\beta(-2\omega; \omega, \omega)$, which is the pertinent property in the present work. This is due to the fact that the $n + 1$ rule allows us to avoid evaluating perturbed densities with respect to nuclear displacements. This is advantageous in cases where a different level of theory is used for determining the molecular force field and the hyperpolarizability gradients for large molecules, because the number of atomic displacements grows linearly with the number of atoms in the molecule, whereas the number of electric-field-perturbed densities that need to be determined remains fixed. In this work, we will, for instance, for the HF calculations use different levels of theory for the force field (B3LYP) and the hyperpolarizability gradients (HF). Moreover, we note that basis set requirements for force fields may differ from those of the hyperpolarizability gradients.

Let us denote a geometrical perturbation arising from the Cartesian displacement of one of the atoms by g, and let f_i denote an electric dipole perturbation i. Furthermore, let $\tilde{\mathcal{E}}_{\mathrm{HF}}$ denote the HF energy, where

$$\tilde{\mathcal{E}}_{\mathrm{HF}} \overset{\{\mathrm{Tr}\}_T}{=} \big(\tilde{\mathbf{h}} - \mathbf{F}\cdot\tilde{\boldsymbol{\mu}} + \tfrac{1}{2}\tilde{\mathbf{G}}^{\gamma}(\tilde{\mathbf{D}})\big)\tilde{\mathbf{D}} + \tilde{h}_{nuc}, \tag{22}$$

so that $\tilde{\mathcal{E}} = \tilde{\mathcal{E}}_{\mathrm{HF}} + \tilde{E}_{\mathrm{xc}}[\tilde{\rho}(\tilde{\mathbf{D}})]$. A given component of the property tensor $\frac{\partial\beta(-2\omega;\omega,\omega)}{\partial g}$ can then be written as

$$L^{gf_1f_2f_3} \overset{\{\mathrm{Tr}\}_T}{=} \mathcal{E}^{gf_1f_2f_3}_{\mathrm{HF}} + E_{\mathrm{xc}}[\rho(\mathbf{D})]^{gf_1f_2f_3} - \mathbf{S}^{g}\mathbf{W}^{f_1f_2f_3}, \tag{23}$$

where

$$\begin{aligned}\mathcal{E}^{gf_1f_2f_3}_{\mathrm{HF}} = {} & \boldsymbol{\mathcal{E}}^{1,gf_1}_{\mathrm{HF}}\mathbf{D}^{f_2f_3} + \boldsymbol{\mathcal{E}}^{1,gf_2}_{\mathrm{HF}}\mathbf{D}^{f_1f_3} + \boldsymbol{\mathcal{E}}^{1,gf_3}_{\mathrm{HF}}\mathbf{D}^{f_1f_2} \\ & + \boldsymbol{\mathcal{E}}^{1,g}_{\mathrm{HF}}\mathbf{D}^{f_1f_2f_3} + \boldsymbol{\mathcal{E}}^{2,g}_{\mathrm{HF}}\mathbf{D}^{f_1f_2}\mathbf{D}^{f_3} + \boldsymbol{\mathcal{E}}^{2,g}_{\mathrm{HF}}\mathbf{D}^{f_1f_3}\mathbf{D}^{f_2} \\ & + \boldsymbol{\mathcal{E}}^{2,g}_{\mathrm{HF}}\mathbf{D}^{f_1}\mathbf{D}^{f_2f_3},\end{aligned} \tag{24}$$

where simplifications due to the fact that some of the contributions are independent of the electric dipole perturbations have been made, and f_1, f_2, and f_3 represent electric dipole perturbations of frequency -2ω, ω, and ω, respectively, and

$$\mathcal{E}^{1}_{\mathrm{HF}} \overset{\{\mathrm{Tr}\}_T}{=} \mathbf{h} - \mathbf{F}\cdot\mu + \mathbf{G}^{\gamma}(\tilde{\mathbf{D}}), \tag{25}$$

$$\mathcal{E}^{2}_{\mathrm{HF}} \overset{\{\mathrm{Tr}\}_T}{=} \mathbf{G}^{\gamma}. \tag{26}$$

The differentiation and subsequent evaluation of $\mathbf{W}^{f_1f_2f_3}$ in Eq. (23) is handled with the use of recursion in the open-ended response property implementation.[11] The appropriate terms can be obtained from a straightforward differentiation of Eq. (13). We will not present here the method for the evaluation of the perturbed density and Fock (and overlap) matrices used in the evaluation of the terms in Eq. (23), but we note that they are readily obtained.[11,16] In the following, we will show how the exchange–correlation contribution $E_{\mathrm{xc}}[\rho(\mathbf{D})]^{gf_1f_2f_3}$ is determined.

C. Exchange–correlation contributions to the gradient of the first hyperpolarizability

We define the XC energy $E_{\mathrm{xc}}[\rho(\mathbf{r})]$ as the integral over a local function $\epsilon_{\mathrm{xc}}(\mathbf{r})$ that depends on the density $n(\mathbf{r})$ and its Cartesian gradient $\nabla n(\mathbf{r})$ according to

$$E_{\mathrm{xc}} = \int \mathrm{d}\mathbf{r}\, \epsilon_{\mathrm{xc}}(n(\mathbf{r}), \nabla n(\mathbf{r})). \tag{27}$$

To simplify the notation, we collect the density variables

$$n(\mathbf{r}) = \sum_{\mu\nu} \Omega_{\mu\nu}(\mathbf{r}) D_{\nu\mu}, \tag{28}$$

and

$$\nabla n(\mathbf{r}) = \sum_{\mu\nu} (\nabla\Omega_{\mu\nu}(\mathbf{r})) D_{\nu\mu}, \tag{29}$$

in a generalized density vector $\rho(\mathbf{r})$. The XC energy and the XC potential matrix in Eq. (18) are integrated on a numerical grid defined by a set of suitably chosen grid points $\mathbf{r}_i$ and grid weights w_i according to

$$E_{\mathrm{xc}} \approx \sum_i w_i \epsilon_{\mathrm{xc}}(\rho(\mathbf{r}_i)), \tag{30}$$

$$(\mathcal{F}_{\mathrm{xc}})_{\mu\nu} \approx \sum_i w_i \frac{\partial \epsilon_{\mathrm{xc}}(\rho(\mathbf{r}_i))}{\partial \rho(\mathbf{r}_i)} \frac{\partial \rho(\mathbf{r}_i)}{\partial D_{\nu\mu}} = \sum_i w_i v_{\mathrm{xc}}(\mathbf{r}_i)(\Omega_\rho)_{\mu\nu}(\mathbf{r}_i). \tag{31}$$

The generalized overlap distribution vector $(\Omega_\rho)_{\mu\nu}$ contains in our case

$$(\Omega)_{\mu\nu} = \chi^*_\mu \chi_\nu, \tag{32}$$

and

$$(\nabla\Omega)_{\mu\nu} = (\nabla\chi^*_\mu)\chi_\nu + \chi^*_\mu(\nabla\chi_\nu), \tag{33}$$

where χ_μ is a Gaussian basis function. When differentiating the XC energy and the XC potential matrix, we ignore the contributions from grid-weight derivatives.

For the implementation of analytic hyperpolarizability gradients using Kohn–Sham DFT, we form the XC energy density derivative $\epsilon_{\mathrm{xc}}^{gf_1f_2f_3}$,

$$\begin{aligned}\epsilon_{\mathrm{xc}}^{gf_1f_2f_3} = {} & \frac{\partial \epsilon_{\mathrm{xc}}}{\partial \rho}\rho^{gf_1f_2f_3} + \frac{\partial^2 \epsilon_{\mathrm{xc}}}{\partial \rho^2}[\rho^g \rho^{f_1f_2f_3} + \rho^{f_1}\rho^{gf_2f_3} \\ & + \rho^{f_2}\rho^{gf_1f_3} + \rho^{f_3}\rho^{gf_1f_2}] \\ & + \frac{\partial^3 \epsilon_{\mathrm{xc}}}{\partial \rho^3}[\rho^g\rho^{f_1}\rho^{f_2f_3} + \rho^g\rho^{f_2}\rho^{f_1f_3} + \rho^g\rho^{f_3}\rho^{f_1f_2} \\ & + \rho^{f_1}\rho^{f_2}\rho^{gf_3} + \rho^{f_1}\rho^{f_3}\rho^{gf_2} + \rho^{f_2}\rho^{f_3}\rho^{gf_1}] \\ & + \frac{\partial^4 \epsilon_{\mathrm{xc}}}{\partial \rho^4}\rho^g\rho^{f_1}\rho^{f_2}\rho^{f_3}.\end{aligned} \tag{34}$$

This expression is not explicitly programmed, but we obtain the contributions directly from the XCFUN program[12,13] by forming a generalized density Taylor series expansion which is internally contracted with the Taylor expansion of the XC functional.

In order to construct the generalized density Taylor series expansions, we evaluate the following generalized perturbed densities for a block of grid points:

$$\rho^f \overset{\mathrm{Tr}}{=} \mathbf{\Omega}_\rho \mathbf{D}^f, \tag{35}$$

$$\rho^{ff} \overset{\mathrm{Tr}}{=} \mathbf{\Omega}_\rho \mathbf{D}^{ff}, \tag{36}$$

$$\rho^{fff} \overset{\mathrm{Tr}}{=} \mathbf{\Omega}_\rho \mathbf{D}^{fff}, \tag{37}$$

$$\rho^g \overset{\mathrm{Tr}}{=} \mathbf{\Omega}^g_\rho \mathbf{D}, \tag{38}$$

$$\rho^{gf} \overset{\mathrm{Tr}}{=} \mathbf{\Omega}^g_\rho \mathbf{D}^f, \tag{39}$$

$$\rho^{gff} \overset{\mathrm{Tr}}{=} \mathbf{\Omega}^g_\rho \mathbf{D}^{ff}, \tag{40}$$

$$\rho^{gfff} \overset{\mathrm{Tr}}{=} \mathbf{\Omega}^g_\rho \mathbf{D}^{fff}. \tag{41}$$

These generalized perturbed densities are internally contracted with the XC functional expansion. This approach is also used to form differentiated v_{xc} contributions.

III. COMPUTATIONAL DETAILS

To illustrate the performance of the code and investigate the importance of electron correlation effects, we consider the hyper-Raman spectra of two isomers of retinal: *all-trans*-retinal and 11-*cis*-retinal. These systems were studied at both the HF and DFT levels of theory using the Turbomole-TZV2P basis set.[19] For DFT, the functionals BLYP,[20–22] B3LYP,[23,24] PBE,[25,26] and PBE0[27] were used. The geometry optimizations of the two systems were carried out using the DALTON quantum chemistry program.[28] The molecular Hessians were calculated at the optimized geometries, from which the harmonic vibrational frequencies and normal modes of the systems were identified. Due to the well-known deficiencies in the prediction of harmonic vibrational frequencies at the HF level of theory, we have for the HF calculations used the B3LYP geometry and B3LYP harmonic frequencies, and we have used the B3LYP normal modes in the transformation of the calculated HF hyperpolarizability Cartesian geometrical derivatives into the normal-mode basis (*vide infra*).

Calculations of the first-order geometrical derivatives of the molecular first hyperpolarizability using Cartesian displacements were carried out using the aforementioned general open-ended response code, which in the present implementation utilizes the general framework of the DALTON program in the determination of, for instance, the perturbed density matrices using the linear response solver of Jørgensen *et al.*[29] One-electron integral contributions were provided by the GEN1INT program.[30,31] Two-electron contributions were obtained using the existing functionality of DALTON. For the DFT calculations, exchange–correlation contributions were provided by the XCFUN program,[12,13] using an in-house integrator. However, the exchange–correlation contribution to the unperturbed density and Fock matrices was calculated using the existing functionality of DALTON. The Cartesian gradients of the first hyperpolarizability were transformed to normal-mode basis and subsequently used for the calculation of hyper-Raman scattering cross sections. For the HF response property calculations, the B3LYP geometries were used, and the B3LYP normal modes were used for the transformation to normal-mode basis, as mentioned above, whereas for the DFT calculations, the response property calculations and normal mode transformations were done with optimized geometries and vibrational analyses using the specific DFT exchange–correlation functional.

IV. RESULTS AND DISCUSSION

Before discussing the HRS spectra, let us first consider the excited states and absorption spectrum of the all-trans-retinal. The experimental absorption spectrum of all-trans-retinal shows a maximum at about 375 nm with a tail extending as far into the long wavelength region as 425 nm.[14] Our

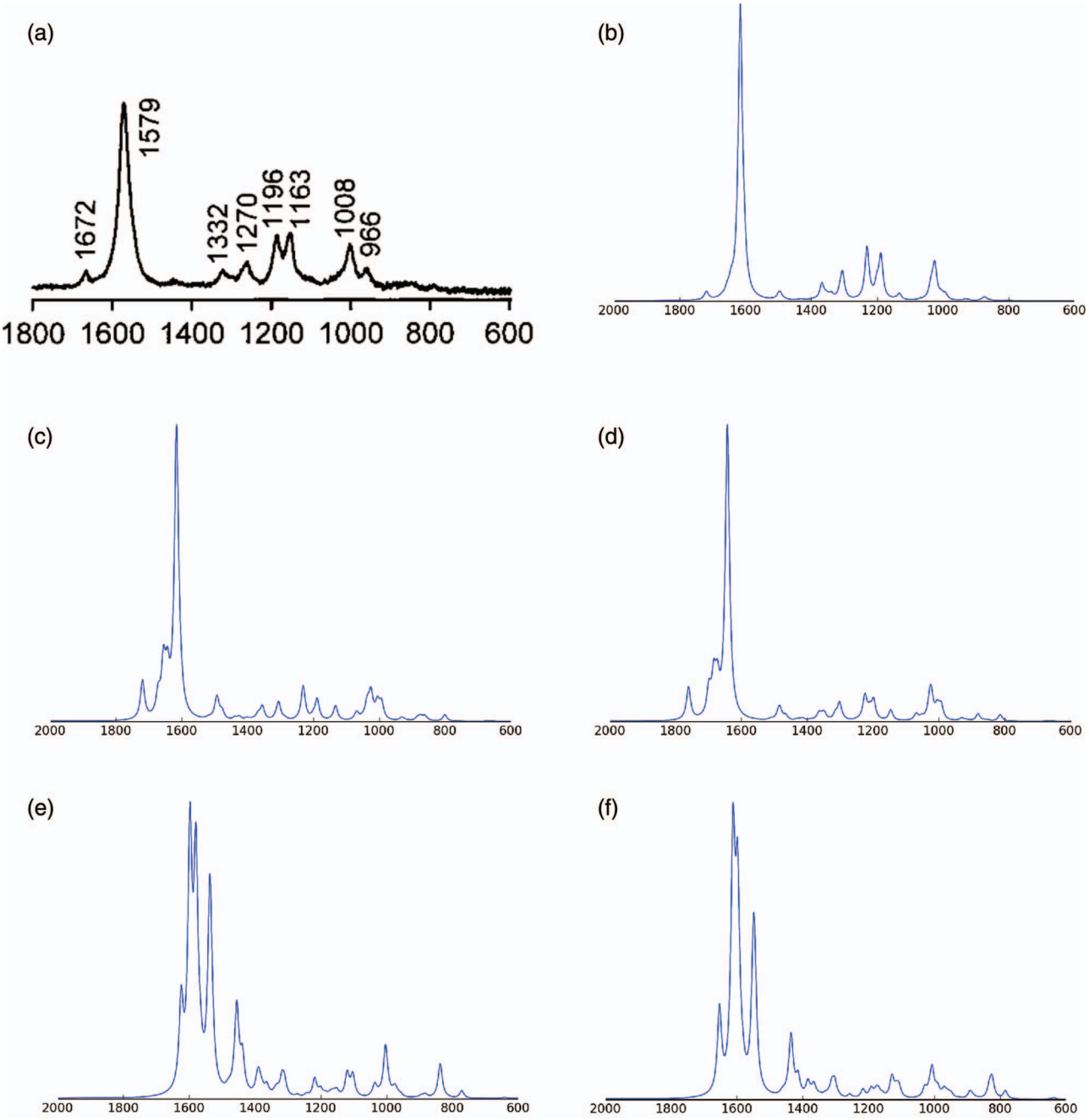

FIG. 1. Hyper-Raman spectra for *all-trans*-retinal: (a) Experimental resonance hR spectrum at room temperature in cyclohexane at an incident wavelength of 800 nm, (b)–(e) Computed spectra at 293 K, incident wavelength 946 nm, VV polarization: (b) B3LYP geometry and vibrational analysis and HF response, (c) B3LYP, (d) PBE0, (e) BLYP, (f) PBE. Each computed spectrum is normalized to highest-intensity peak and uses a FWHM of 15 cm^{-1}. Frequency axis in cm^{-1}. The experimental results are adapted with permission from Mizuno *et al.*, J. Phys. Chem. A **106**, 3599 (2002). Copyright (2002) American Chemical Society.

DFT calculations all predict two low-lying excited states, of which one of the states is one-photon forbidden. In the case of the hybrid functionals B3LYP and PBE0, the lowest state at about 420 nm (417 nm and 420 nm for B3LYP and PBE0, respectively) has a high oscillatory strength, whereas for the non-hybrid functionals, the second state absorbs strongly at 502 nm for both BLYP and PBE. The underestimation of the excitation energies for the non-hybrid functionals and the (slight) overestimation of the excitation energies for the hybrid functionals is in agreement with the expected performance of DFT in predicting excitation energies.[32,33] Indeed, to some extent the hybrid functionals perform better than could have been expected for such a highly conjugated system as all-trans-retinal, as we see no signs of the hyperpolarizability breakdown often observed with non-hybrid or hybrid functionals for conjugated systems.[34]

Since our theoretical calculations show that the first absorption band corresponds to an isolated electronic state, the tail observed in the experimental absorption spectrum is due to either vibronic or solvent effects. Indeed, the experimental HRS profiles at the double wavelength show no signs of resonance for wavelengths longer than 790–800 nm. As such, the experimental HRS spectra recorded at 800 nm are off-resonance HRS spectra and well suited for comparison with

our calculated spectra if these are also calculated off resonance. Because of the errors in our calculated excitation energies, our calculations would display two-photon resonance effects at an excitation energy of 800 nm, and we have for this reason calculated the HRS spectra for incident wavelengths of 946 and 1064 nm, respectively, corresponding to a dual-wavelength laser based on Nd:YAG and Nd:YVO_4 crystals, respectively.[35]

In Figure 1, the results of the hyper-Raman calculations assuming VV polarization for a wavelength of 946 nm are shown for *all-trans*-retinal. Included in the figure is also the experimental HRS spectrum in cyclohexane, obtained at an incident wavelength of 800 nm. We have also performed calculations assuming HV polarization and observe no significant differences in the calculated relative scattering cross sections, though there are differences in the absolute scattering cross sections. As our calculations are performed without taking solvent effects into consideration, there are limitations on how directly we can compare the theoretical and experimental spectra. Nevertheless, the comparison may give some indication of the accuracy that can be expected for different computational levels.

From Fig. 1 we see that there is, to a somewhat varying extent, qualitative agreement between experiment and our theoretical results, both for HF and DFT, irrespective of the choice of XC functional. It is worth noting that the HF results are closest to experiment, being almost in quantitative agreement with the experimental results. However, this is likely to be fortuitous, and may be due to accidental cancellation of errors arising, for instance, from the neglect of solvent effects. We emphasize that these results have been obtained using B3LYP harmonic vibrational frequencies, and the accuracy probably would be poorer had the HF normal modes been used instead.

Of the DFT functionals, the functionals that include orbital exchange (B3LYP and PBE0) show the best agreement with experiment. Indeed, the largest difference between the B3LYP and the HF results is the appearance of a high-frequency shoulder (not observed experimentally) on the strongly scattering vibrational band around 1600 cm^{-1} in the B3LYP calculations. In the case of the non-hybrid generalized gradient approximation (GGA) functionals used (BLYP and PBE), the agreement is at best qualitative. For these functionals, several strong features appear around 1600 cm^{-1}, observed neither experimentally nor for the HF and hybrid functional results, and the agreement with experiment for lower-frequency features is also poorer than for the HF and hybrid functional calculations. The origin of these differences could either be in the calculated harmonic force field[11] or be due to near-resonance effects since the second and one-photon active excited state at 502 nm corresponds to an incoming one-photon wavelength of about 1000 nm for these GGA functionals. Nevertheless, these results suggest that the non-hybrid GGA functionals are not suitable for reproducing the hyperpolarizability gradients needed for the calculation of the hyper-Raman scattering cross sections.

DFT has been shown to have problems for calculating electric hyperpolarizabilities of conjugated systems.[34] However, it has been shown that these problems can to a large extent be mitigated by the use of long-range-corrected functionals.[36] The good agreement between our B3LYP and PBE0 results and experiment for the HRS spectra suggests that hybrid functionals are capable of accounting for the changes in the electronic structure of the molecule as probed by the HRS scattering cross sections. This may be due to the fact that the HRS scattering cross section probes the variation in the first hyperpolarizability during a vibrational motion and not the first hyperpolarizability itself. Thus, even though

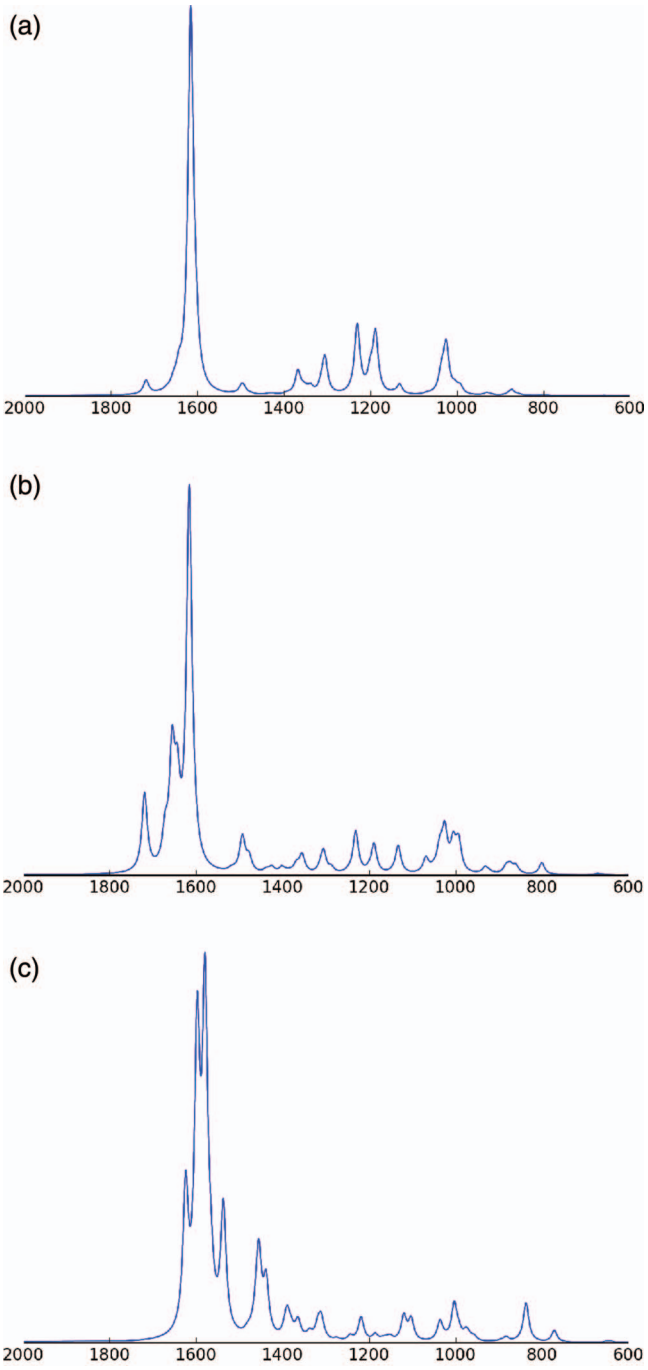

FIG. 2. Hyper-Raman spectra for *all-trans*-retinal: (a)–(c) Computed spectra at 293 K, incident wavelength 1062 nm, VV polarization: (a) B3LYP geometry and vibrational analysis and HF response, (b) B3LYP, (c) BLYP. Each spectrum is normalized to its highest-intensity peak and uses a FWHM of 15 cm^{-1}. Frequency axis in cm^{-1}.

TABLE I. Intensities, frequencies, and classification of the normal modes of *all-trans*-retinal that have strongest intensities in the computed hyper-Raman spectra at the HF and DFT (B3LYP) level. Frequencies from the DFT/B3LYP vibrational analysis. Intensities given as the percentage of the mode with the strongest intensity at the same level of theory. Results reported for an incident wavelength of 946 nm using VV polarization.

Mode	Freq. (cm^{-1})	Int. (HF)	Int. (B3LYP)	Motion
1	1719	2.8	13.4	Terminal HCC angle bend
2	1671	0.4	7.3	Ring C–C stretch
3	1655	2.3	17.7	Carbon backbone bond length alternation
4	1643	4.1	13.4	Carbon backbone bond length alternation (mainly alkene)
5	1616	100.0	100.0	Carbon backbone bond length alternation (mainly alkene)
6	1604	9.4	4.7	Carbon backbone bond length alternation (mainly alkene)
7	1493	0.9	6.5	Ring methyl scissor motion
8	1368	5.5	2.0	Alkene HCC angle bend
9	1355	1.2	4.7	Alkene HCC angle bend
10	1305	9.3	6.1	Alkene HCC angle bend
11	1231	17.0	11.7	Alkene HCC angle bend
12	1200	4.9	1.1	Complete backbone bond length alternation
13	1188	14.6	7.2	Complete backbone bond length alternation
14	1133	2.1	5.1	Complete backbone bond length alternation
15	1037	3.2	4.5	Methyl torsion
16	1025	11.7	8.9	Methyl torsion
17	1005	1.6	4.2	H out-of-plane wiggle (with some methyl wiggle)
18	992	1.6	4.9	H out-of-plane wiggle (with strong methyl wiggle)

the first hyperpolarizability itself may be overestimated by DFT, the changes in the hyperpolarizability during a vibrational motion are qualitatively correct, thus leading to good results for the calculated HRS scattering cross sections.

In Figure 2, results for *all-trans*-retinal in the VV polarization obtained with an incident wavelength of 1064 nm are presented. We note that only minor differences compared to the 946 nm results of Figure 1 can be seen, suggesting that the choice of frequency for the incident light under nonresonant conditions only has a minor effect on the spectral intensities. However, there are changes in the relative intensities of the (artificial) bands that in the DFT calculations constitute the spectral features around 1600 cm^{-1} in the case of BLYP, even changing which peak in this band is the most intense. From Eq. (6), we note that the intensity scales as $(\omega - \omega_a)^4$, suggesting that for even longer wavelengths of the incident light, the relative intensity of the peaks would be expected to favor low-energy vibrational transitions due to the quenching of the high-energy modes, assuming that the hyperpolarizability derivatives do not change significantly, which is not expected as electronic resonances are less likely for longer wavelengths of the incident light.

TABLE II. Intensities, frequencies, and classification of the normal modes of 11-cis-retinal that have strongest intensities in the computed hyper-Raman spectra at the HF and DFT (B3LYP) level. Frequencies from the DFT/B3LYP vibrational analysis. Intensities given as the percentage of the mode with the strongest intensity at the same level of theory. Results reported for an incident wavelength of 946 nm using VV polarization.

Mode	Freq. (cm^{-1})	Int. (HF)	Int. (B3LYP)	Motion
1	1717	3.5	15.1	Terminal HCC angle bend
2	1670	0.9	9.1	Carbon backbone bond length alternation
3	1651	2.3	36.0	Carbon backbone (alkene) bond length alternation
4	1633	8.1	9.7	Carbon backbone (alkene) bond length alternation
5	1610	100.0	100.0	Carbon backbone (alkene) bond length alternation
6	1587	4.9	4.9	Carbon backbone (alkene) bond length alternation
7	1492	1.4	6.4	Ring methyl scissor motion
8	1480	6.4	4.4	Alkene HCC angle bend
9	1379	14.8	9.6	Alkene HCC angle bend
10	1311	12.0	9.4	Alkene HCC angle bend
11	1236	13.3	12.0	Alkene HCC angle bend
12	1163	6.2	3.8	Complete backbone bond length alternation
13	1112	4.7	10.3	Carbon backbone shift/bond length alternation
14	1044	8.3	10.1	Methyl torsion
15	1030	5.4	3.8	Methyl torsion
16	1010	6.4	3.5	Methyl torsion
17	1000	3.5	9.4	H out-of-plane wiggle

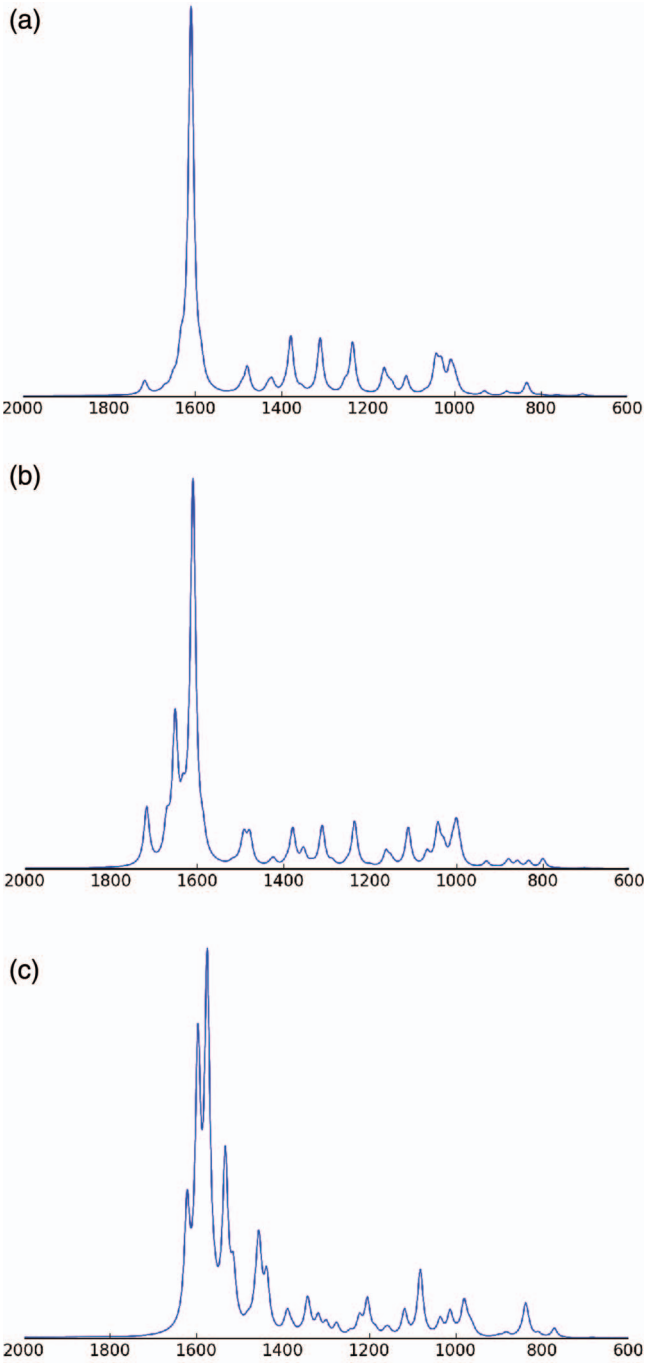

FIG. 3. Hyper-Raman spectra for 11-*cis*-retinal: (a)–(c) Computed spectra at 293 K, incident wavelength 946 nm, VV polarization: (a) B3LYP geometry and vibrational analysis and HF response, (b) B3LYP, (c) BLYP. Each spectrum is normalized to its highest-intensity peak and uses a FWHM of 15 cm^{-1}. Frequency axis in cm^{-1}.

In Tables I and II, we have collected and classified the normal modes of *all-trans*- and *11-cis*-retinal that have the largest intensities in the calculated hyper-Raman spectra in Figures 1–3. It is clear that the majority of the most intense bands arise from vibrations involving the conjugation pathways. In the cases involving methyl group torsions or hydrogen wiggles, these are also attached to the conjugation pathway.

For 11-*cis* retinal, there are no experimental results to which we can compare our computed results. Nevertheless, considering the importance of this structural isomerism in biological systems,[37] it is of interest to explore to what extent HRS will be sensitive to these structural differences. We report our calculated results at the HF, B3LYP, and BLYP levels of theory at a wavelength of $\omega = 946$ nm with VV polarization in Figure 3. The computed spectra show roughly the same variation in features as the corresponding spectra for the *all-trans* isomer. Using the HF results as a basis for comparison, we note that the spectra for the two isomers are fairly similar, except for the 1000–1400 cm^{-1} region which appears more sensitive to the structural characteristics of the two isomers and thus might be used as a fingerprint region. However, for the most interesting, dominant HRS cross sections, the intensity pattern remains invariant to the cis/trans isomerism for all functionals, further supporting that this insensitivity to cis/trans-isomerism in a conjugated backbone may be a general characteristic of the HRS spectra.

V. CONCLUDING REMARKS

We have presented the first analytic implementation and calculations of the gradients of the first electronic hyperpolarizability at the density-functional level of theory. We have used a recent implementation of the open-ended, atomic-orbital-based quasienergy derivative framework of Thorvaldsen *et al.*[16] implemented using recursive programming techniques.[11] In combination with a flexible scheme for evaluating differentiated one- and two-electron integrals[30,31,38,39] and derivatives of the exchange–correlation functionals based on automatic differentiation,[12] this allows for a very flexible framework for the evaluation of high-order molecular properties.

We have applied the new code to the study of the hyper-Raman spectra of *all-trans* and 11-*cis* retinal. The best agreement with the experimental, resonant HRS spectrum is obtained using B3LYP vibrational analysis in combination with HF hyperpolarizability gradient calculations, transforming the HF hyperpolarizability Cartesian gradients to the normal-mode basis using the B3LYP normal modes, and using these transformed quantities in the calculation of the HRS cross sections. However, the high level of agreement shown for this method is likely to be accidental, and may in part be due to cancellation of errors stemming from our neglect of anharmonicities and solvent effects. Nevertheless, the rather minor differences observed between the HF and B3LYP results suggest that correlation effects, as described by DFT, in general are rather modest for the HRS cross sections, assuming that the B3LYP vibrational analysis is used with the HF hyperpolarizability gradients as done in this work. This finding lends support to the quality of the results and conclusions drawn in earlier studies in the literature using HF HRS intensities.[5,8–10] The performance of the non-hybrid GGA functionals BLYP and PBE is in general poorer, but the origin of this poorer performance is not clear. It has previously been noted that the quality of harmonic frequencies and normal modes calculated with GGAs in general is worse than those obtained using hybrid functionals.[40] However, using the B3LYP force field with the BLYP hyperpolarizability gradients (not shown) does not lead to qualitative improvements, suggesting that the

GGA hyperpolarizability gradients are of poorer quality than hybrid functionals (and Hartree–Fock) when compared to the experimental observations.

The hyper-Raman spectra of the two isomers are quite similar, but show differences in the 1000–1400 cm^{-1} region. Nevertheless, it is not likely that HRS will be a very attractive approach for the study of isomerism in these molecules. The lack of structural specificity in the HRS spectra of these retinal molecules is due to the fact that the HRS cross sections are governed by a property that largely probes the conjugation pathways during the molecular vibrations, and the cis/trans-isomerism in the middle of the conjugated backbone does not induce large changes in the conjugation pathways and thus the gradient of the first hyperpolarizability.

The availability of analytic geometrical derivatives of the first hyperpolarizability also enables the exploration of pure vibrational corrections to higher-order polarization properties such as the second hyperpolarizability. We note that correlation effects have been found to be significant for pure vibrational contributions to the first hyperpolarizability,[34,41–45] suggesting that the availability of these analytic derivatives at the DFT level of theory are more important for pure vibrational corrections than for the case of HRS cross sections.

ACKNOWLEDGMENTS

This work has received support from the Research Council of Norway through a Centre of Excellence Grant (Grant No. 179568/V30) and a research grant (Grant No. 191251), the European Research Council through a ERC Starting Grant (Grant No. 279619), and from the Norwegian Supercomputer Program through a grant of computer time (Grant No. NN4654K). U.E. acknowledges support from the European Research Council under the European Union (EU) Seventh Framework Program through the Advanced Grant ABACUS, ERC Grant Agreement No. 267683.

[1] J. C. Decius and J. E. Rauch, Ohio State Symposium on Molecular Structure and Spectroscopy, Paper 48, 1959.
[2] R. W. Terhune, P. P. Maker, and C. M. Savage, Phys. Rev. Lett. **14**, 681 (1965).
[3] A. M. Kelley, Annu. Rev. Phys. Chem. **61**, 41 (2010).
[4] W. P. Acker, D. H. Leach, and R. K. Chang, Chem. Phys. Lett. **155**, 491 (1989).
[5] A. Mohammed, H. Ågren, M. Ringholm, A. J. Thorvaldsen, and K. Ruud, Mol. Phys. **110**, 2315 (2012).
[6] V. Kopecký and V. Baumruk, Chemické listy **105**, 162 (2011).
[7] V. Rodriguez, D. Talaga, F. Adamietz, J. L. Bruneel, and M. Couzi, Chem. Phys. Lett. **431**, 190 (2006).
[8] O. Quinet and B. Champagne, J. Chem. Phys. **117**, 2481 (2002).
[9] O. Quinet, B. Champagne, and V. Rodriguez, J. Chem. Phys. **121**, 4705 (2004).
[10] O. Quinet, B. Champagne, and V. Rodriguez, J. Chem. Phys. **124**, 244312 (2006).
[11] M. Ringholm, D. Jonsson, and K. Ruud, J. Comput. Chem. **35**, 622 (2014).
[12] U. Ekström, L. Visscher, R. Bast, A. J. Thorvaldsen, and K. Ruud, J. Chem. Theory Comput. **6**, 1971 (2010).
[13] U. Ekström, XCFun library, 2010, see http://repo.ctcc.no/projects/xcfun.
[14] M. Mizuno, H. Hamaguchi, and T. Tahara, J. Phys. Chem. A **106**, 3599 (2002).
[15] S. J. Cyvin, J. E. Rauch, and J. C. Decius, J. Chem. Phys. **43**, 4083 (1965).
[16] A. J. Thorvaldsen, K. Ruud, K. Kristensen, P. Jørgensen, and S. Coriani, J. Chem. Phys. **129**, 214108 (2008).
[17] T. Helgaker and P. Jørgensen, Theor. Chim. Acta **75**, 111 (1989).
[18] K. Kristensen, P. Jørgensen, A. J. Thorvaldsen, and T. Helgaker, J. Chem. Phys. **129**, 214103 (2008).
[19] A. Schäfer, C. Huber, and R. Ahlrichs, J. Chem. Phys. **100**, 5829 (1994).
[20] A. D. Becke, Phys. Rev. A **38**, 3098 (1988).
[21] C. T. Lee, W. T. Yang, and R. G. Parr, Phys. Rev. B **37**, 785 (1988).
[22] S. H. Vosko, L. Wilk, and M. Nusair, Can. J. Phys. **58**, 1200 (1980).
[23] A. D. Becke, J. Chem. Phys. **98**, 5648 (1993).
[24] P. J. Stephens, F. J. Devlin, C. F. Chabalowski, and M. J. Frisch, J. Phys. Chem. **98**, 11623 (1994).
[25] J. P. Perdew, K. Burke, and M. Ernzerhof, Phys. Rev. Lett. **77**, 3865 (1996).
[26] J. P. Perdew, K. Burke, and M. Ernzerhof, Phys. Rev. Lett. **78**, 1396 (1997).
[27] C. Adamo and V. Barone, J. Chem. Phys. **110**, 6158 (1999).
[28] Dalton 2011, an *ab initio* electronic structure program, 2011, see http://www.daltonprogram.org.
[29] P. Jørgensen, H. J. A. Jensen, and J. Olsen, J. Chem. Phys. **89**, 3654 (1988).
[30] B. Gao, A. J. Thorvaldsen, and K. Ruud, Int. J. Quantum Chem. **111**, 858 (2011).
[31] B. Gao and A. J. Thorvaldsen, GEN1INT Version 0.2.1, 2012, Gen1Int is a library to evaluate the derivatives of one-electron integrals with respect to the geometry perturbation, external electric and magnetic fields, and total rotational angular momentum at zero fields with contracted rotational London atomic orbitals, and is released under the GNU Lesser General Public License.
[32] M. J. G. Peach, P. Benfield, T. Helgaker, and D. J. Tozer, J. Chem. Phys. **128**, 044118 (2008).
[33] M. J. G. Peach, C. R. Le Sueur, K. Ruud, M. Guillaume, and D. J. Tozer, Phys. Chem. Chem. Phys. **11**, 4465 (2009).
[34] B. Champagne, E. A. Perpete, S. J. A. van Gisbergen, E. J. Baerends, J. G. Snijders, C. Soubra-Ghaoui, K. A. Robins, and B. Kirtman, J. Chem. Phys. **109**, 10489 (1998).
[35] C. Y. Cho, C. C. Chang, and Y. F. Chen, Laser Phys. Lett. **10**, 045805 (2013).
[36] T. Yanai, D. P. Tew, and N. C. Handy, Chem. Phys. Lett. **393**, 51 (2004).
[37] C. Dugave and L. Demange, Chem. Rev. **103**, 2475 (2003).
[38] S. Reine, E. I. Tellgren, and T. Helgaker, Phys. Chem. Chem. Phys. **9**, 4771 (2007).
[39] A. J. Thorvaldsen, CGTO-Diff-ERI, 2012, A library for the evaluation of geometry-differentiated 2e-integrals (d^n/dR_k^n), released under the GNU Lesser General Public License.
[40] M. Ringholm, D. Jonsson, R. Bast, B. Gao, A. J. Thorvaldsen, U. Ekström, T. Helgaker, and K. Ruud, J. Chem. Phys. **140**, 034103 (2014).
[41] P. Sałek, O. Vahtras, T. Helgaker, and H. Ågren, J. Chem. Phys. **117**, 9630 (2002).
[42] P. Sałek, T. Helgaker, O. Vahtras, H. Ågren, D. Jonsson, and J. Gauss, Mol. Phys. **103**, 439 (2005).
[43] D. Jacquemin, E. A. Perpéte, G. Scalmani, M. J. Frisch, R. Kobayashi, and C. Adamo, J. Chem. Phys. **126**, 144105 (2007).
[44] H. Sekino, Y. Maeda, M. Kamiya, and K. Hirao, J. Chem. Phys. **126**, 014107 (2007).
[45] B. Gao, M. Ringholm, R. Bast, A. J. Thorvaldsen, K. Ruud, and M. Jaszuński, J. Phys. Chem. A **118**, 748 (2014); **118**, 2835–2837 (2014) (Erratum).